4A.3 STUDIES OF PHASED-ARRAY SCAN STRATEGIES FOR RADAR DATA ASSIMILATION

Qin Xu[1]*, Huijuan Lu[2], Li Wei[2], Qingyun Zhao[3]

[1]NOAA/National Severe Storms Laboratory, Norman, Oklahoma
[2]Cooperative Institute for Mesoscale Meteorological Studies, University of Oklahoma
[3]Naval Research Laboratory, Monterey, California

1. INTRODUCTION

Sponsored by multi-government agencies and especially by the US Navy, a phased-array weather radar has been constructed at NSSL Norman Oklahoma. This establishes the first National Weather Radar Testbed (NWRT) equipped with the solid-state phased-array antenna (Forsyth et al. 2005). One of the important and yet very challenging research goals at NWRT is to optimally design and utilize the electronically-controlled agile beam scans for various meteorological applications. This includes assimilating phased-array radar observations into mesoscale models to improve numerical analyses and predictions of severe storms and other hazardous weather conditions. To this end, this paper intends to address the following two basic issues: (i) how to measure information content extracted from radar observations by an optimal 4D analysis; and (ii) how to balance radar observation accuracy with observation spatial and temporal resolutions to optimally design phased-array scans for a 4D assimilation system. These issues are important for measuring and taking the full advantages of phased-array rapid and flexible scan capabilities in data assimilation. The first issue is addressed theoretically in the next section. The second issue is examined numerically in section 3.

2. MEASURING INFORMATION FROM OBSERVATIONS

2.1 *Review of Recent Results*

When observations are assimilated into a numerical weather prediction (NWP) model by an optimal analysis, the background state is provided by the NWP model prediction valid at the analysis time. As shown in Xu (2007), the information extracted from radar observations by an analysis can be measured by the relative entropy defined by $R(p, q) = \int d\mathbf{x} p(\mathbf{x}) \ln[p(\mathbf{x})/q(\mathbf{x})]$, where $q(\mathbf{x})$ is the background probability density function (pdf), $p(\mathbf{x})$ is the analysis pdf and $\mathbf{x}$ is the state vector. For Gaussian pdfs, this gives

$$R(p, q) = (\mathbf{a} - \mathbf{b})^T \mathbf{B}^{-1} (\mathbf{a} - \mathbf{b})/2 + [\ln\mathrm{Det}(\mathbf{B}\mathbf{A}^{-1}) + \mathrm{Tr}(\mathbf{A}\mathbf{B}^{-1}) - n]/2, \quad (1)$$

where $\mathbf{b}$ is the background mean, $\mathbf{a}$ is the analysis mean, $\mathbf{B}$ is the background covariance matrix, $\mathbf{A}$ is the analysis covariance matrix, $(\ )^T$ denotes the transpose of ( ), Det( ) denotes the determinant of ( ), Tr( ) denotes the trace of ( ), and n is the dimension of $\mathbf{b}$. The first and second terms on the right-hand side of (1) are the signal and dispersion parts of the information content, respectively.

For an optimal analysis (Jazwinski 1970), $\mathbf{a} = \mathbf{b} + \mathbf{B}\mathbf{H}^T(\mathbf{H}\mathbf{B}\mathbf{H}^T + \mathbf{R})^{-1}\mathbf{d}$ and $\mathbf{A}^{-1} = \mathbf{B}^{-1} + \mathbf{H}^T\mathbf{R}^{-1}\mathbf{H}$ or, equivalently, $\mathbf{A} = \mathbf{B} - \mathbf{B}\mathbf{H}^T(\mathbf{H}\mathbf{B}\mathbf{H}^T + \mathbf{R})^{-1}\mathbf{H}\mathbf{B}$, where $\mathbf{R}$ is the observation error covariance matrix, $\mathbf{H}$ is the tangent-linearization of the observation operator $H(\ )$ at $\mathbf{x} = \mathbf{b}$, $\mathbf{d} = \mathbf{y} - H(\mathbf{b})$ is the innovation vector; and $\mathbf{y}$ is the observation vector. Substituting these relationships into (1) gives

$$R(p, q) = \sum[d'_i{}^2 \lambda_i{}^2/(1+\lambda_i{}^2)^2 + \ln(1+\lambda_i{}^2) - \lambda_i{}^2/(1+\lambda_i{}^2)]/2. \quad (2)$$

Here, d'_i is the i-th element of $\mathbf{d}' = \mathbf{U}^T\mathbf{R}^{-1/2}\mathbf{d}$; $\mathbf{U}$ is the left orthogonal matrix given by the singular value decomposition (SVD) of the scaled observation operator: $\mathbf{M} = \mathbf{R}^{-1/2}\mathbf{H}\mathbf{B}^{1/2} = \mathbf{U}\mathbf{\Lambda}\mathbf{V}^T$; λ_i is the i-th diagonal element of the diagonal matrix $\mathbf{\Lambda}$; and the summation is over i from 1 to $r = \mathrm{rank}(\mathbf{M})$. In (2), the observation space is transformed by $\mathbf{U}^T\mathbf{R}^{-1/2}$. In this transformed observation space, the information content becomes separable between components associated with different singular values of $\mathbf{M}$. This leads to the following two important points:

(a) Observations can be compressed into surper-observations by applying the truncated transformation $\mathbf{I}_s\mathbf{U}^T\mathbf{R}^{-1/2}$ to $\mathbf{y}$. The super-observation vector is given by $\mathbf{y}_s = \mathbf{I}_s\mathbf{U}^T\mathbf{R}^{-1/2}\mathbf{y}$, where $\mathbf{I}_s$ is the $s \times s$ identity matrix that projects R^m onto R^s ($s < m$) and m is the dimension of $\mathbf{y}$. This compression causes no information loss as long as $s \geq r = \mathrm{rank}(\mathbf{M})$.

(b) If $\mathbf{y}_s = \mathbf{I}_s\mathbf{U}^T\mathbf{R}^{-1/2}\mathbf{y}$ is further truncated to $s < r$, then the compression will cause an information loss. The

* Corresponding author address: Qin Xu, National Severe Storms Laboratory, 120 David L. Boren Blvd., Norman, OK 73072-7326; E-mail: Qin.Xu@noaa.gov

dispersion part of the information loss caused by the SVD-based compression is the minimum loss for a given truncation number s ($< r$). The signal part of the information loss depends on the truncated non-zero singular values and associated components of **d**'.

The above results, along with the illustrative examples with real radar observations presented in Xu (2007), suggest that the information content extracted by an optimal analysis from radar observations depends on how well the observations are resolved by the analysis. If high-resolution radar observations are poorly resolved by the analysis (due to lack of fine structures in the background covariance and/or insufficient resolution in the analysis grid), then there can be a significant degree of information redundancy (for an optimal lower-resolution analysis in comparison with a higher-resolution one) or observation resolution redundancy (for an optimal analysis with a given background covariance on a given grid). However, the above formulations were derived for spatial analyses. To measure information content gained from phased-array radar rapid scans, we need to consider the temporal dimension in addition to the spatial dimensions and extend the formulations for 4D analyses. Such extensions are derived in the next sub-section.

2.2 *Extended Formulations For 4D Analyses*

The time window for a 4D analysis can cover, say, J observation time levels (at t_j for $j = 1, 2, \ldots J$) between the initial time level (at t_0) and ending time level (at t_J). For simplicity, the forward prediction model is assumed to be linear (or tangent-linearized) and is given by

$$\mathbf{x}_j = \mathbf{F}_j\mathbf{x}_{j-1} + \mathbf{q}_j \quad \text{for } j = 1, 2, \ldots J, \tag{3}$$

where $\mathbf{F}_j$ is the forward operator, $\mathbf{x}_j$ is the state vector at t_j, and $\mathbf{q}_j$ denotes the integrated model error from t_{j-1} to t_j. The tangent-linearized observation model is given by

$$\mathbf{d}_j = \mathbf{H}_j\Delta\mathbf{x}_j + \mathbf{e}_j \quad \text{for } j = 1, 2, \ldots J, \tag{4}$$

where $\mathbf{d}_j = \mathbf{y}_j - H(\mathbf{b}_j)$, $\Delta\mathbf{x}_j = \mathbf{x}_j - \mathbf{b}_j$, $\mathbf{y}_j$ is the observation vector at t_j, $\mathbf{b}_j$ is the background forecast mean state vector at t_j, $\mathbf{H}_j$ is the tangent-linearization of $H_j(\ )$ at $\mathbf{x}_j = \mathbf{b}_j$, $H_j(\ )$ is the observation operator at t_j, and $\mathbf{e}_j$ denotes the observation error at t_j.

The state vector for the 4D state fields over the analysis time window can be represented by the extended state vector: $\mathbf{x}^o = (\mathbf{x}_0^T, \mathbf{x}_1^T, \ldots \mathbf{x}_J^T)^T$. With this extension, (1) and its initial condition can be written into $\mathbf{x}^o = \mathbf{F}^o\mathbf{z}$, where $\mathbf{z} = (\mathbf{x}_0^T, \mathbf{q}_1^T, \ldots \mathbf{q}_J^T)^T$ and $\mathbf{F}^o$ is a $(J + 1)\times(J + 1)$ lower-triangle block matrix operator with the jth diagonal block given by $\mathbf{I}_n$ (the identity matrix in R^n) and the jkth block (at the jth row and kth column) given by $\mathbf{F}_j\mathbf{F}_{j-1}\ldots\ \mathbf{F}_k$ for $k < j$ (below the block-diagonal) and by zero for $k > j$ (above the block-diagonal). Without the initial condition, (1) can be written into $\mathbf{x} = \mathbf{F}\mathbf{z}$, where $\mathbf{x} = (\mathbf{x}_1^T, \mathbf{x}_2^T, \ldots \mathbf{x}_J^T)^T$ and $\mathbf{F}$ is a $J\times(J + 1)$ block matrix operator reduced from $\mathbf{F}^o$ by removing the first row of blocks. The background covariance for $\mathbf{z}$ is a block diagonal matrix given by $\mathbf{Q} = \text{diag}\{\mathbf{B}, \mathbf{Q}_1, \ldots \mathbf{Q}_J\}$, where $\mathbf{Q}_j$ is the covariance matrix of $\mathbf{q}_j$ and the vector components of $\mathbf{z} = (\mathbf{x}_0^T, \mathbf{q}_1^T, \ldots \mathbf{q}_J^T)^T$ are assumed to be not cross-correlated. The background covariance for $\mathbf{x}$ is then given by $\mathbf{FQF}^T$.

Similarly, the background forecast mean vector and mean vector can be extended and denoted by $\mathbf{b} = (\mathbf{b}_1^T, \mathbf{b}_2^T, \ldots \mathbf{b}_J^T)^T$ and $\mathbf{a} = (\mathbf{a}_1^T, \mathbf{a}_2^T, \ldots \mathbf{a}_J^T)^T$, respectively. The extended innovation vector is $\mathbf{d} = (\mathbf{d}_1^T, \mathbf{d}_2^T, \ldots \mathbf{d}_J^T)^T$. The extended observation error covariance matrix is $\mathbf{R} = \text{diag}\{\mathbf{R}_1, \mathbf{R}_2, \ldots \mathbf{R}_J\}$. With the above extensions, the costfunction and related solutions for an optimal 4D analysis can be cast into the same matrix forms as for an optimal 3D analysis (Courtier 1997; Lorenc 2003), so similar information entropy formulations can be derived for an optimal 4D analysis as the above (1) and (2). If $\mathbf{x}$ is taken to be the control vector, then the extended tangent-linear observation operator is given by $\mathbf{H} = \text{diag}\{\mathbf{H}_1, \mathbf{H}_2, \ldots \mathbf{H}_J\}$. If $\mathbf{z}$ is taken to be the control vector, then the extended tangent-linear observation operator is given by $\mathbf{HF}$. In either case, the extended form for the scaled observation operator [used in the derivation of (2)] is always given by

$$\mathbf{M} = \mathbf{R}^{-1/2}\mathbf{HFQ}^{1/2}. \tag{5}$$

Thus, by using the SVD of the extended $\mathbf{M}$ in (5), the singular-value form of the relative entropy in (2) can be similarly derived and used to measure the information extracted from 4D observations by an optimal 4D analysis.

2.3 *Remarks*

(a) According to (1), the information content extracted from observations by an optimal analysis can be measured only indirectly in terms of the analysis increment (defined by $\mathbf{a} - \mathbf{b}$) and pdf changes (from q to p) produced by the analysis, so the information content depends on both the observation and background pdfs.

(b) In 3D variational data assimilation, $\mathbf{B}$ and $\mathbf{R}$ are pre-estimated and not updated with assimilation cycles. If the estimation problem is nearly linear and the observation operator $\mathbf{H}$ is also fixed in time, then as pointed out by Sean Healy (private communication

from ECMWF), the expectation of the signal term (computed by averaging in time) reduces to $[n - \mathrm{Tr}(\mathbf{AB}^{-1})]/2$. Thus, on average, the signal term cancels the last two terms in the second (dispersion) part on the righthand side of (1) and the relative entropy reduces to the Shannon entropy difference: $S(q) - S(p) = (1/2)\ln\mathrm{Det}(\mathbf{BA}^{-1})$. In this case, the relative entropy provides no advantage in measuring the averaged information content. However, for each individual batch of observations (used in each data assimilation cycle), the relative entropy can have some advantages in measuring the information content (as shown in Xu 2007), especially if the background covariance is flow-dependent (as in the Kalman filter).

(c) $\mathbf{M}$ in (5) has $J \times m$ columns and $(J + 1) \times n$ rows. This matrix operator is much larger than the already very large $m \times n$ matrix operator $\mathbf{M}$ in the original (2). The rank of $\mathbf{M}$ in (5) is also enlarged, so more information can be extracted from the 4D observations. However, if the model is perfect (with $\mathbf{q}_j = 0$ for $j = 1, 2, \ldots J$), then $\mathbf{M}$ reduces to its first block column of sub-matrices in which the jth sub-matrix is given by $\mathbf{R}_j^{-1/2}\mathbf{H}_j\mathbf{F}_j\mathbf{F}_{j-1}\ldots\mathbf{F}_1\mathbf{B}^{1/2}$. In this case, rank($\mathbf{M}$) can become too low to extract additional information from the 4D observations. Equivalently and intuitively, we can envision that the perfect model operator maps the 4D observations into 3D observations with much enhanced density in 3D, so the information redundancy or observation resolution redundancy can be easily revealed in the 3D space.

(d) When the model errors are correlated in time, a decrease (or increase) in model error correlations will increase (or decrease) the information extracted from the 4D observations. This property is envisioned based on the point made and scenario discussed in (c).

(e) Information from observations can be redundant (or insufficient) for an optimal analysis if the observations have excessive (or inadequate) spatial and/or temporal resolutions and coverage. According to (2) and (5), an increase in observation accuracy should increase the information content for an optimal analysis. This, however, is not always true and the impact of observation accuracy can even become negative for analyses produced by a practically used sub-optimal assimilation system (such the ensemble Kalman filter) in which the background covariance is not accurately estimated. This problem is examined numerically in the next section.

3. EXPERIMENTS ON OPTIMAL SCAN CONFIGURATIONS

One of the major advantages of the phased array radar is the capability to adaptively scan weather phenomena at high temporal resolution (1 min or less per volume scan). Regardless this and other possible gains, there is always a limit on the number of independent samples acquirable per unit time for a given phased array radar (or any other radar). This imposes an overall constraint on radar observation accuracy and resolutions. Under this constraint, an increase in accuracy (or resolution) will cause a decrease in resolution (or accuracy) and, by the same token, a resolution increase in one spatial or temporal dimension will cause a resolution decrease in another dimension (without compromising the accuracy). Because of this, there should be a proper balance or trade-off between observation accuracy and resolutions when radar scans are configured to improve storm-scale radar wind analyses and data assimilation. This problem will be studied by performing assimilation experiments with model simulated radar radial-velocity observations of a supercell storm. In particular, we will examine the impacts of observation accuracy and resolutions on the assimilated storm winds by the ensemble square-root filter (EnSRF) (Whitaker and Hamill 2002). The quality of the assimilation will be evaluated by the root mean square (RMS) error of the analyzed wind field.

3.1 *Simulated Radar Observations and Assimilation System*

a. Prediction model and simulated storm

The Advanced Regional Prediction System (ARPS, Xue et al. 2001) is used for both simulation and analysis. The ARPS contains 12 prognostic variables plus the turbulent kinetic energy (TKE) used by the 1.5-order subgrid-scale turbulent closure scheme. All of these prognostic state variables except for TKE are subject to updating at each analysis step of assimilation.

The physical domain is $64 \times 64 \times 16$ km^3 for all experiments. The model grid for the "true" comprises of $131 \times 131 \times 35$ grid points (with horizontal grid spacing $\Delta x = \Delta y = 0.5$ km and vertical grid spacing $\Delta z = 0.5$ km), while the grid is coarsened to $35 \times 35 \times 35$ grid points (with $\Delta x = \Delta y = 2$ km and $\Delta z = 0.5$ km) for all the assimilation experiments. Thus, the forecast model is imperfect. The "true" state is generated by a model simulation initialized from a modified Del City sounding for the classic May 29, 1977 Del City, Oklahoma supercell storm case as in Tong and Xue (2005, referred to as TX05 hereafter).

b. Simulated radar observations

Simulated radar radial-velocity observations are produced by interpolating the simulated "true" velocities to observation points, projecting along radar beams and then adding with random errors to drawn from a normal distribution with zero mean and a

specified standard deviation. All the observation points are in the radar polar coordinates, and each volume scan contains 14 tilts at the elevation angles of 0.48, 1.45, 2.4, 3.3, 4.3, 5.2, 6.2, 7.5, 8.7, 10.0, 12, 14.0, 16.7 and 19.5 degree. On each tilt, the benchmark horizontal resolutions are 1° in the azimuthal direction and 0.5 km in the radial direction. The benchmark temporal resolution is 5 min per volume. The radial-velocity data are assumed to be available only in the precipitation regions, where the reflectivity exceeds 10 dBZ. The reflectivity is calculated from the hydrometeor mixing ratios from the 'true' simulation as in TX05. The ground-based radar is located at the southwest corner of the computational domain, that is, at the coordinate origin, for all experiments.

Assume that the gross errors (due to by range folding, velocity aliasing, and non-meteorological clutters) are removed by data quality controls (e.g., Gong et al. 2003; Zhang et al. 2005; Liu et al. 2005), so random errors in radar radial-velocity measurements (level-II data) are caused mainly due to inhomogeneities of velocity and reflectivity within each sampling volume. The error standard deviation may have a lower bound of about $\sigma = 1$ m s^{-1} in a fair-weather turbulent boundary layer (see section 9.1.1.2 of Doviak and Zrnic 1993). By reformulating the conventional innovation method, Xu et al. (2007) estimated radar radial-velocity observation error and background velocity error covariance from time series of radar radial-velocity innovation (observation minus independent background), and the estimated observation error standard deviation is $\sigma = 4$ m s^{-1}. This estimate ($\sigma = 4$ m s^{-1}) will be used with the above lower bound ($\sigma = 1$ m s^{-1}) to examine how the EnKF analysis is impacted by a change in observation accuracy.

c. Data assimilation procedure

The observation errors are assumed to be uncorrelated (or de-correlated), so the serial algorithm of EnSRF (Whitaker and Hamill 2002) can be used conveniently. In this EnSRF, the Kalman gain matrix reduces to a column vector (for single-observation analysis). A simple trilinear interpolation is used in the observation operator H. The ensemble has 40 members ($N = 40$). As in TX05, the initial ensemble forecasts are started at the 20 min of model time by adding random noises to a prior background state which is horizontally homogeneous and described by the environmental sounding in the vertical. The random noises are sampled from normal distributions with zero mean and standard deviation of 3 m s^{-1} for u, v and w, and 3 K for potential temperature. The pressure, moisture and microphysical variables are not perturbed initially. The observations are assimilated every $\tau = 5$ minutes. The first analysis is performed at $t = 25$ min. After 15 more assimilation cycles, the last analysis is performed at the end ($t = T = 100$ min) of the last (16^{th}) cycle. In all the experiments, the covariance localization radius is set to 8 km and the inflation factor is set to $\beta = 1.07$.

3.2 *Experiments with Different Observation Accuracies*

a. Experiment design

In this section, two (one control and one test) EnSRF assimilation experiments are designed and performed with simulated high-resolution radial-velocity data (0.5 km in radial range and 1° in azimuth) of different accuracies. The model error is not estimated or treated explicitly except that the inflation factor is set to $\beta = 1.07$ to partially account for the enhanced forecast error due to the imperfect model. By settings the error standard deviations to (i) $\sigma = 1$ m s^{-1} and (ii) $\sigma = 4$ m s^{-1}, two sets of observations are generated. These two sets are denoted by Oτ1 and Oτ4, respectively (see the first two rows of Table 1). As explained earlier, $\sigma = 1$ m s^{-1} is an estimated lower bound of σ, while $\sigma = 4$ m s^{-1} is a statistical estimate obtained by Xu et al. (2007). The Oτ4 will be used in the control experiment, denoted by Eτ4. The Oτ1 will be used in the test experiment, denoted by Eτ1.

Table 1. Observation error variances and resolutions for six sets of model-simulated radar radial-velocity data. All the data contain 14 tilts at the elevation angles of 0.48, 1.45, 2.4, 3.3, 4.3, 5.2, 6.2, 7.5, 8.7, 10.0, 12, 14.0, 16.7 and 19.5 degree.

data set	σ^2 (m/s)^2	Radial (km)	Azimuth (degree)	Temporal (min)
Oτ1	1	0.5	1	5
Oτ4	4^2	0.5	1	5
O2km5min	2^2	2	1	5
O4km5min	1	4	2	5
O2km2min	10	2	1	2
O2km1min	20	2	1	1

b. Evaluation parameters

(i) The analysis quality is evaluated by the RMS error of the ensemble mean velocity field. For the ith model variable, denoted by x_i, the analysis RMS error is defined by

$$\sigma_i \equiv \{| \overline{x}_i - x_i^t|^2\}_p^{1/2}, \quad (6)$$

where $\overline{x}_i$ denotes the ensemble mean background forecast (or analysis) of x_i before (or immediately

after) each analysis time, x_i^t denotes the "true" value of x_i, and $\{\ \}_p$ denotes the average over the grid points covered by the observations (where the reflectivity > 10 dBZ).

(ii) The RMS error averaged for the three velocity components at the end ($t = T = 100$ min) of the assimilation is denoted and defined by

$$\sigma_v \equiv \{\sigma_i|_{t=T}\}_3, \tag{7}$$

where $\{\ \}_3$ denotes the average over i (= 1, 2, 3) for the three velocity components (u, v, w).

(iii) To quantify the accuracy of the ensemble mean in the test experiment relative to that in the control experiment, it is convenient to introduce and define the relative RMS error (RRE) as follows:

$$\text{RRE} \equiv \sigma_v/\sigma_{v\text{E}\tau4}, \tag{8}$$

where $\sigma_{v\text{E}\tau4}$ denotes the values of σ_v in the control experiment Eτ4.

(iv) The spatially averaged ensemble spread of x_i is defined by

$$s_i \equiv \{\overline{|x_i - \bar{x}_i|^2}\}_p^{1/2}, \tag{9}$$

and s_i^2 is the spatially averaged ensemble variance of x_i over the regions covered by the observations.

(v) Ideally, the ensemble spread in each variable should satisfy a consistency relationship with the ensemble-mean RMS error. This consistency relation requires the ratio between the ensemble spread and the ensemble-mean RMS error to be statistically equal to $[N/(N+1)]^{1/2}$ (Murphy 1988). For the ith variable x_i, this ratio is defined and denoted by

$$r_i \equiv s_i/\sigma_i. \tag{10}$$

We call it the consistency ratio (the ith variable). For the ensemble size ($N = 40$) used in this study, the ideal value for the consistency ratio is $[N/(N+1)]^{1/2} = 0.988$.

(vi) The consistency ratio averaged for the three velocity components at the end ($t = T$) of the assimilation is defined and denoted by

$$r_v \equiv \{r_i|_{t=T}\}_3, \tag{11}$$

If the uncertainty of the ensemble mean is well quantified by the ensemble spread, then r_i should be statistically equal to $[N/(N+1)]^{1/2}$ according to the consistency relationship. Since the initial ensemble members are generated in the same way at the beginning of the assimilation in all the experiments, the consistency ratio is initially the same for each variable in all the experiments. After the initial time, however, the ratio will undergo different variations over the assimilation period in different experiments.

Table 2. σ_v RRE and CPU time ratios from five test experiments with respect to those from the control experiment Eτ4.

Experiment	σ_v (m/s)	RRE	r_v	CPU ratio
Eτ1	4.04	1.08	0.08	1.00
Eτ4	3.73	1	0.23	1
E2km5min	3.56	0.95	0.31	0.24
E4km5min	4.35	1.17	0.31	0.06
E2km2min	3.36	0.90	0.62	0.66
E2km1min	4.35	1.17	1.08	1.12

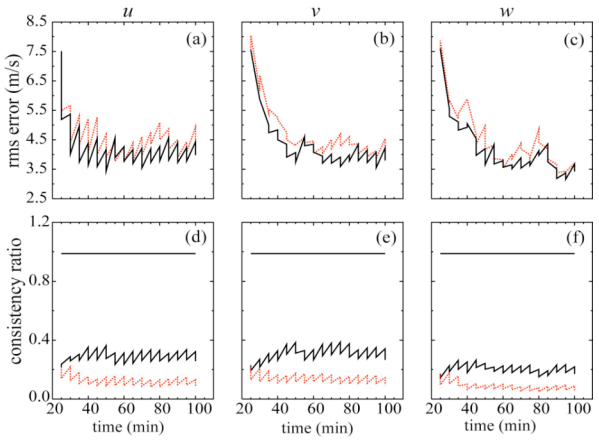

Fig. 1. The RMS errors of ensemble mean forecasts and analyses (a)-(c), and the consistency ratios (d)-(f) for u, v and w in Eτ4 (black lines) and Eτ1 (red lines). Units are shown in the plots. The ideal value for the consistency ratio, that is $[N/(N+1)]^{1/2} = 0.988$ for $N = 40$, is marked by the straight horizontal lines in (d)-(f).

c. Results and discussions

The computed values of σ_v, RRE and r_v from the test experiment Eτ1 are listed in the first row of Table 2 in comparison with those from the control experiment Eτ4 (in the second row). As listed, when the observation error is reduced from $\sigma = 4$ m s^{-1} (in Eτ4) to 1 m s^{-1} (in Eτ1), the RRE is increased by 8% and the averaged consistency ratio r_v is decreased dramatically from 0.23 to 0.08. The ensemble mean RMS errors σ_i and consistency ratios r_i are plotted as functions of time over the 16 assimilation cycles in Figs. 1a-c and 1d-f, respectively, for (u, v, w) from the two experiments. As shown, Eτ1 (red lines) performs

worse than Eτ4 (black lines) although the data set Oτ1 is more accurate than Oτ4. Figures 1d-f show that the consistency ratios in Eτ1 are initially the same as in Eτ4 but decrease in the first few assimilation cycles and then stay far below the ideal value (0.988) during the subsequent assimilation cycles. This indicates that the ensemble spread in Eτ1 is too small to quantify the uncertainty of the ensemble mean, and the insufficient spread is responsible for the poor performance of Eτ1 relative to Eτ4.

The "true" fields of vertical velocity and horizontal perturbation wind at z = 6 km are plotted in a time series in the first row of Fig. 2 against the ensemble mean analyses from Eτ1 (the second row) and Eτ4 (the third row). As shown, the gross pattern of the true wind field is reasonably well assimilated (after five cycles) in these two experiments. However, since the model is imperfect and has a coarsened resolution from the "true", the assimilated updrafts in Eτ1 and Eτ4 are slightly weaker than the "true". The major updraft patterns in Eτ4 are closer to the "true" pattern than in Eτ1. This result shows again that the analysis is not improved but becomes slightly worse as the observation error is reduced from σ = 4 m s^{-1} (in Eτ4) to 1 m s^{-1} (in Eτ1).

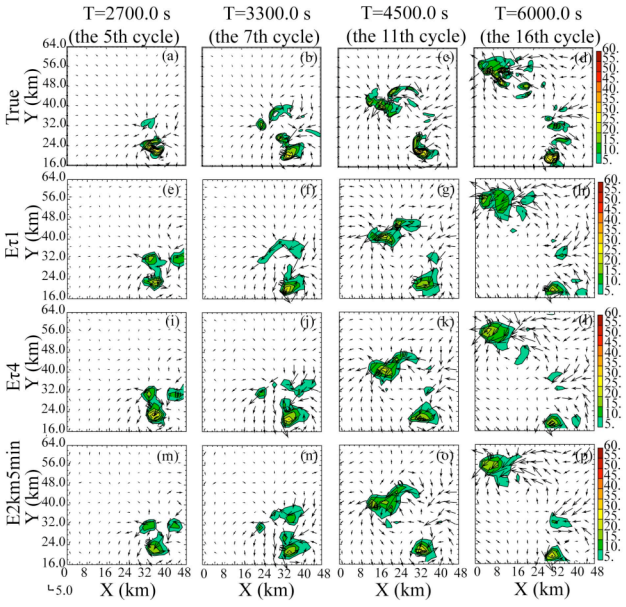

Fig. 2. Vertical velocity (contours and colors at intervals of 5 m s^{-1} and ≥ 5 m s^{-1}) and horizontal perturbation wind (vectors plotted every other grid point) at level z = 6 km: (a)–(d) "true" simulation; and analyses from (e)–(h) Eτ1, (i)–(l) Eτ4, (m)–(p) E2km5min, at the 5th, 7th, 11th and 16th cycle during the assimilation period. The vector scale for the horizontal wind is shown by the arrow (5 m s^{-1}) at the lower-left corner.

The above results show that when the radar data spatial resolution is excessively higher than the grid resolution, an increase in data accuracy does not necessarily improve the EnSRF analysis. When the observations are significantly more accurate than the ensemble mean, further increasing the true observation accuracy (without inflating the estimated σ) can actually deteriorate the EnSRF analysis. This negative impact is counter-intuitive but not surprising, because the background covariance is not accurate as it is estimated from an ensemble of merely 40 imperfect-model predictions.

The negative impact of the increased data accuracy on the assimilation in Eτ1 is caused by errors and noises in the covariance (estimated from an ensemble of 40 imperfect-model predictions) and the smallness of σ^2 in the denominator of the Kalman gain (not shown). As the observations are much denser than the model grid at least in the radial direction along each radar beam, the analysis (applied serially to all the observations) tends to excessively reduce the spread without adequately reducing the mean RMS error in observation-covered regions. This causes the poor performance of Eτ1. The problem cannot be alleviated by the convention inflation of covariance (or spread) because the excessively reduced spread is caused by the smallness of σ^2 and the reduced spread is localized mainly in observation-covered regions. Note that the inflation factor is already set to 1.07 in Eτ1. A further increase of this factor can only worsen the situation according to our additional experiments (not shown). On the contrary, the problem can be actually alleviated when the inflation factor is reduced from 1.07 to 1 (that is, with no inflation). In this case, the RRE in Eτ1 is reduced by 8% (from 1.08 to 1.00).

The background variance (estimated by the ensemble spread) and observation error variance are two competing terms in the Kalman gain and β factor (not shown). This implies that the above problem can be alleviated by inflating the observation error variance. This is indeed true as indicated by our additional experiments. For example, when σ is inflated from 1 to 4 m s^{-1} in the Kalman gain and β factor (but the true observation error standard deviation remains to be σ = 1 m s^{-1}), the RRE in Eτ1 is reduced by 15% (from 1.08 to 0.93) and the spread is also improved (since the averaged consistency ratio r_v is increased from 0.08 to 0.25). This inflation is approximately optimal for Eτ1, and it changes the impact of observation accuracy from negative (-8%) to positive (7%) in reducing the analysis RRE. Thus, when observations are excessively accurate and dense while the background covariance is not accurately estimated (from a small ensemble of imperfect-model predictions), the EnSRF analysis becomes not really sensitive to the true observation error but sensitive to

how σ is specified and inflated. In this case, how to optimally inflating σ will depend on the observation resolutions and the excessiveness of the observation accuracy versus the inaccuracy of the estimated background covariance. The problem, however, is not further explored here, because inflating σ is not the best choice as long as the radar scans can be configured (or re-configured) to avoid (or eliminate) excessive measurement accuracy. For this reason, we will consider Oτ4 only and use it as a benchmark data set to study trade-offs between observation accuracy and resolutions in the next section.

3.3 *Trade-Offs Between Observation Accuracy & Resolutions*

a. A idealized simple rule for trade-offs

The number of acquirable samples of weather echoes per unit time always has a limit for a given radar, especially if the radar performs multifunction tasks (such as the phased array radar does). Constrained by this limit, if the observation resolution is increased, say, by n times in one spatial or temporal dimension, then the observation error variance will increase likely also by about n times (because the error variance of an estimate is inversely proportional to the number of independent samples used to yield the estimate according to the well-known central limit theorem in statistics). Therefore, as a simple rule for considering trade-offs between observation accuracy and resolutions in our experiment design, the observation error variance σ^2 will decrease (or increase) by n times if the observation resolution is decreased (or increased) by n times in any spatial or temporal dimension.

Using the above rule, radar scans can be configured with different trade-offs between accuracy and resolutions from the benchmark data set Oτ4. As we have seen in the previous section, Oτ4 has the same spatial resolutions as Oτ1 and thus may also have excessive spatial resolutions as Oτ1 does. Based on this consideration, four sets of observations (denoted by O2km5min, O4km5min, O2km2min and O2km1min) are generated from Oτ4 by reducing the spatial resolutions in favor of increasing the accuracy and temporal resolution. Their observation error variances and resolutions are listed in the last four rows of Table 1.

It is necessary to point out that the above simple rule for trade-offs between observation accuracy and resolution is an idealized situation. In reality, radar sampled (level I) velocities are not truly independent, and the statistical properties of random meteorological scatterers are not precisely stationary in each resolution volume. Consequently, when the observation resolution increases (or decreases) in a single spatial or temporal dimension, the trade-off will yield a smaller increase (or decrease) in the true observation error variance than estimated by the simple rule. These complications are not considered in this study.

b. Trade-offs between accuracy and spatial resolutions

Two test assimilation experiments are performed with O2km5min and O4km5min, and these experiments are denoted by E2km5min and E4km5min, respectively. The control experiment is Eτ4. The parameter values of σ_v, RRE and r_v from E2km5min and E4km5min are listed in the third and fourth rows of Table 2, respectively, in comparison with those from Eτ4 (in the second row). In addition, the CPU time ratios (with respect to the CPU time used by Eτ4) are listed in the last column. As listed in Tables 1 and 2, when the radial resolution is coarsened from 0.5 to 2 km and thus σ is reduced from 4 m s^{-1} (in Eτ4) to 2 m s^{-1} (in E2km5min), the RRE is decreased by 5% (from 1 to 0.95), the averaged consistency ratio r_v is increased from 0.23 to 0.31, and the CPU time ratio is reduced from 1 to 0.24. However, when the radial resolution is further coarsened to 4 km, and the azimuthal resolution is coarsened from 1 to 2 degree in E4km5min (and thus σ is further reduced to 1 m s^{-1}), the analysis becomes worse and the RRE is increased by 17% (from 1 to 1.17) although the averaged consistency ratio r_v remains to be 0.31 and the CPU time ratio is further reduced to 006. The worsened analysis accuracy in E4km5min is caused by the excessively coarsened spatial resolutions. Judging from the analysis accuracy, E2km5min outperforms Eτ4 and E4km5min, and the observation set O2km5min provides the optimal trade-off among the three.

The ensemble mean RMS errors σ_i and consistency ratios r_i are plotted as functions of time over the 16 assimilation cycles in Figs. 3a-c and 3d-f, respectively, for (u, v, w) from the two test experiments E2km5min and E4km5min versus those from the control experiment Eτ4. As shown in Figs. 3a-c, E2km5min (pink lines) performs better than Eτ4 (black lines) and E4km5min (green lines) performs significantly worse than Eτ4. Figures 3d-f show that the averaged consistency ratios in E2km5min and E4km5min are initially the same as in Eτ4 but become higher than that in Eτ4 during the subsequent assimilation cycles. This indicates that the ensemble spreads are improved in E2km5min and E4km5min although their averaged consistency ratios are still significantly below the ideal value (0.988). These results are consistent with those in Table 2.

The ensemble mean fields of vertical velocity and horizontal perturbation wind from E2km5min are plotted at z = 6 km in a time series in the last row of Fig. 2 in comparison with the "true" fields (in the first

row) and from Eτ4 (the third row). As shown, after the 5th analysis cycle, the locations and gross patterns of the two main updrafts are better retrieved in E2km5min and closer to the "true" than those in the control experiment Eτ4. This result shows again that the analysis is improved by the trade off that coarsens the radial resolution from 0.5 km (in Oτ4) to 2 km (in O2km5min) in favor of increasing the observation accuracy.

As we have seen, by assimilating O2km5min instead of the original Oτ4 which has quadruply higher radial resolution than O2km5min, the computational cost can be reduced quadruply. This trade-off also improves the analysis accuracy in addition to the computational efficiency. After the spatial resolutions are optimally selected, the EnSRF analysis can be further improved by a proper trade-off between the accuracy and temporal resolution. This problem is explored in the next subsection.

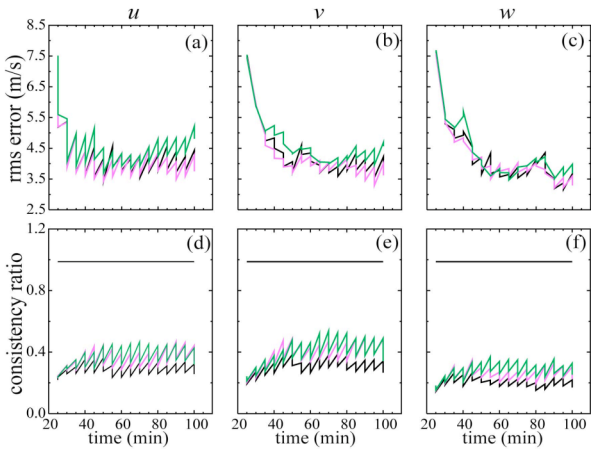

Fig. 3. As in Fig. 1 but for Eτ4 (back lines), E2km5min (pink lines) and E4km5min (green lines).

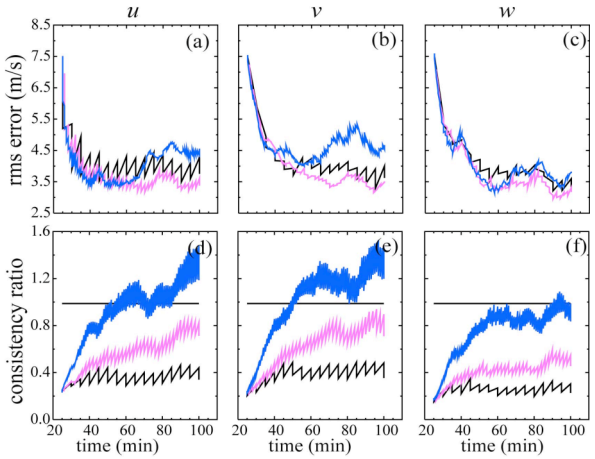

Fig. 4. As in Fig. 1 but for E2km5min (black lines), E2km2min (pink lines) and E2km1min (blue lines).

c. Trade-offs between accuracy & temporal resolution

In this subsection, two test experiments are performed with O2km2min and O2km1min, and these experiments are denoted by E2km2min and E2km1min, respectively. Because O2km2min and O2km1min have the same spatial resolutions as O2km5min, comparisons will be made with respect to E2km5min instead of Eτ4 [although the RRE is still computed relative to Eτ4 according to the definition in (8)]. The parameter values of σ_v, RRE, r_v and CPU time ratio from E2km2min and E2km1min are listed in the last two rows of Table 2 in comparison with those from E2km5min. As listed in Tables 1 and 2, when the temporal resolution is refined from 5 to 2 min and thus τ is increased from 2 to $10^{1/2}$ m s^{-1} in E2km2min, the RRE is decreased by 5% (from 0.95 to 0.90) and the averaged consistency ratio r_v is doubled to 0.62, but the CPU time ratio is increased from 0.24 to 0.66. When the temporal resolution is further refined to 1 min and thus σ is increased to $20^{1/2}$ m s^{-1} in E2km1min, the CPU time ratio is further increased to 1.12. The analysis, however, becomes worse and the RRE is increased by 27% (from 0.90 to 1.17), although the averaged consistency ratio r_v is increased to 1.08.

The ensemble mean RMS errors σ_i and consistency ratios r_i are plotted as functions of time over the 16 assimilation cycles in Figs. 4a-c and 4d-f, respectively, for (u, v, w) from E2km2min and E2km1min versus those from E2km5min. As shown in Figs. 4a-c, E2km2min (pink lines) outperforms E2km5min (black lines) and E2km1min (blue lines) significantly underperforms E2km5min. Figures 4d-f show that the averaged consistency ratios in E2km2min and E2km1min are initially the same as in E2km5min but become much higher than those in E2km5min during the subsequent assimilation cycles. Although the consistency ratios become close to the ideal value, the analysis is worsened in E2km1min. Judging from the analysis accuracy, E2km2min outperforms E2km5min and E2km1min, and the observation set O2km2min provides the optimal trade-off among the three (O2km5min, O2km2min and O2km1min). As the observation accuracy is reduced in favor of enhancing the temporal resolution in O2km2min, inflating σ become more harmful to the assimilation in E2km2min than in E2km5min.

Note that the consistency relationship can be used to evaluate only a part of the quality of the estimated covariance. Moreover, the consistency ratio defined in (10) is merely a ratio averaged over regions covered by the observations. When this ratio is close to the ideal value of $[N/(N+1)]^{1/2}$, the averaged variance part of the estimated covariance is close to the averaged RMS error of the ensemble mean. However, the covariance is not free of spurious noisy structures

when it is estimated from a small ensemble of imperfect-model predictions. The covariance localization can suppress distant spurious structures but it will also suppress the true structures and cause some imbalances in the EnSRF analysis with respect to the model dynamics and physics. If the observations are made and assimilated into the model at an excessively high frequency, then the ensemble integration will be interrupted by the analysis and thus contaminated by the analysis-introduced spurious structures and imbalances too frequently to stay the correct trajectories and faithfully represent the evolution of the true prediction probability distribution. In this case, the averaged spread can be close to the ideal value but the covariance is poorly estimated. This explains the worsened analysis in E2km1min.

3.4 *Summary*

The results of the assimilation experiments are summarized as follows:

(a) The EnSRF analysis can be negatively impacted if the true observation error is overly reduced (say, from $\sigma = 4$ to 1 m s^{-1} for level-II velocity data) but the estimated observation error is not inflated in the EnSRF. This negative impact occurs when the observations have excessive accuracy and resolutions while the background covariance is not accurately estimated (from 40 imperfect-model predictions in this study). In this case, unless the estimated observation error is properly inflated, the analysis (applied serially to all the observations) tends to excessively reduce the spread without adequately reducing the ensemble mean error in regions densely covered by the observations. This causes the negative impact.

(b) When the true observations have no excessive accuracy, the analysis can be improved by properly reducing the observation resolution (to 2 km in the radial direction) in favor of increasing the observation accuracy, and there is an optimal trade-off between the accuracy and spatial resolutions.

(c) When the spatial resolutions are optimally selected, the analysis can be further improved by properly enhancing the temporal resolution of radar volume scans (from every 5 to 2 min) at the price of reducing the observation accuracy, and there is an optimal trade-off between observation accuracy and temporal resolution.

The above summarized results should be useful for optimally configuring radar scans (especially phased-array radar scans at the NWRT) to improve storm-scale radar wind assimilation, although the trade-offs between observation accuracy and resolutions considered in this study is based on an idealized rule (see section 3.3a). The quantitative aspects of the results will likely change if the model grid resolutions become significantly different from those used in this study. For example, if the horizontal grid spacing is reduced further (say, from $\Delta x = 2$ to 0.2 km for the purpose of resolving and analyzing tornadic vortices within a storm), then the optimal trade-off will likely be balanced at higher spatial and temporal resolutions but lower observation accuracy than shown in this study, provided that the trade-off is made with respect to the same benchmark observations (that is, Oτ4 to the full capabilities of the radar) as considered here. In this case, the EnSRF may behave quite differently than shown in this study. This speculation needs to be verified by future studies.

Acknowledgments. The original ARPS EnKF code was kindly provided by Mingjing Tong and Ming Xue. The computational resource was provided by the OU Supercomputing Center for Education & Research at the University of Oklahoma. The research work was supported by the FAA contract IA# DTFA03-01-X-9007 to NSSL and by ONR Grant N000140410312 to CIMMS, the University of Oklahoma. Funding was also provided to CIMMS by NOAA/Office of Oceanic and Atmospheric Research under NOAA-University of Oklahoma Cooperative Agreement #NA17RJ1227, U.S. Department of Commerce.

REFERENCES

Courtier, P., 1997: Dual formulation of four dimensional variational assimilation. *Quart. J. Roy. Meteor. Soc.*, **123**, 2449–2461.

Doviak, J. D. and Zrnic, D. S. 1993: *Doppler Radar and Weather Observations*. Second Edition. Academic Press, New York, 562 pp.

Forsyth, D. E., J. F. Kimpel, D. S. Zrnic, R. Ferek, J. F. Heimmer, T. J. McNellis, J. E. Crain, A. M. Shapiro, R. J. Vogt, and W. Benner, 2005: The national weather radar testbed (Phased-Array). *32nd Conference on Radar Meteorology*, 24-29 October 2005, Albuquerque, New Mexico, Amer. Meteor. Soc., 12R.3.

Gong, J., Wang L. and Xu, Q. 2003: A three-step dealiasing method for Doppler velocity data quality control. *J. Atmos. & Oceanic Technol.*, **20**, 1738-1748.

Jazwinski, A. H. 1970. *Stochastic Processes and Filtering Theory*. Academic Press, 376 pp.

Liu, S., Q. Xu, and P. Zhang, 2005: Quality control of Doppler velocities contaminated by migrating

birds. Part II: Bayes identification and probability tests. *J. Atmos. Oceanic Technol.* **22**, 1114-1121.

Lorenc, A. C., 2003: Modeling of error covariances by 4D-Var data assimilation. *Quart. J. Roy. Meteor. Soc.*, **129**, 3167-3182.

Murphy, J. M., 1988: The impact of ensemble forecasts on predictability. *Quart. J. Roy. Meteor. Soc.*, **114**, 463–493.

Tong, M., and M. Xue, 2005: Ensemble Kalman filter assimilation of Doppler radar data with a compressible nonhydrostatic model: OSS experiments. *Mon. Wea. Rev.*, **133**, 1789–1807.

Whitaker, J. S., and T. M. Hamill, 2002: Ensemble data assimilation without perturbed observations. *Mon. Wea. Rev*, **130**, 1913–1924.

Xue, M., Coauthors, 2001: The Advanced Regional Prediction System (ARPS)—A multiscale nonhydrostatic atmospheric simulation and prediction tool. Part II: Model physics and applications. *Meteor. Atmos. Phys.*, **76**, 143–165.

Xu, Q., 2007: Measuring information content from observations for data assimilation: Relative entropy versus Shannon entropy difference. *Tellus*, 59A, 198-209.

Xu, Q., K. Nai, and L. Wei, 2007: An innovation method for estimating radar radial-velocity observation error and background wind error covariances. *Quart. J. Roy. Meteor. Soc.*, **133**, 407-415.

Zhang, P., Liu, S. and Xu, Q. 2005: Quality control of Doppler velocities contaminated by migrating birds. Part I: Feature extraction and quality control parameters. *J. Atmos. Oceanic Technol.*, **22**, 1105-1113.